Thermal Analysis of Engine Inlet Anti-Icing Systems

Kamel M. Al-Khalil,* Theo G. Keith, Jr.,† and Kenneth J. DeWitt‡
University of Toledo, Toledo, Ohio 43606
James K. Nathman§
Analytical Methods, Inc., Redmond, Washington 98052
and
Donald A. Dietrich¶
General Electric Company, Cincinnati, Ohio 45215

A hot-air anti-icing system of a gas turbine engine inlet is analyzed numerically. A three-dimensional potential flow code, which accounts for compressibility effects, is used to determine the flowfield in and around the inlet. A particle trajectory code is developed using a local linearization technique. The trajectory code is used to calculate local water-impingement rates. Energy balances are performed on both the surface runback water and the metallic skin to determine their temperature distributions. A variety of test cases are considered in order to validate the various numerical components of the process as well as to demonstrate the procedure.

Nomenclature

A = area or cross-sectional area
C_D = drag coefficient of a droplet
C_p = specific heat
D = diameter
F = force acting on a droplet
F = wetness factor
f = friction factor at the cowl surface
g = acceleration of gravity
g_c = conversion factor
h_i = heat-transfer coefficient between the hot air and the inner surface of the cowl
h_w = heat-transfer coefficient between the outer surface of the cowl and the runback water
h_∞ = heat-transfer coefficient between the freestream and the outer surface of the cowl
J = mechanical equivalent of heat
K = thermal conductivity
LWC = liquid water content
L_f = latent heat of fusion of water
L_v = latent heat of vaporization of water
M = molecular mass, Mach number
MED = droplets mean effective diameter
m = mass
m^o = runback water mass flow rate
P = static pressure
Pr = Prandtl number
S = wrap distance
Sc = Schmidt number
T = temperature
T^* = reference temperature
t = thickness or time
V, V, v = velocity
W = rate of water mass flux
x = wrap distance from the cowl nose highlight
Y = local perimeter of the nacelle
β = collection efficiency
γ = specific heat ratio of air
η_r = recovery factor of air temperature
μ = dynamic viscosity
ρ = density
τ_w = shear stress at the cowl surface
ϕ = relative humidity

Subscripts

a = anti-ice air
d = droplet
e = local value at edge of boundary layer
evap = evaporating from the cowl outer surface
i = inner surface of the cowl
imp = impingement on the cowl outer surface
o = outer surface of the cowl
p = panel
sk = metal skin
v = saturated vapor
vap = vapor
v, w = saturated vapor at temperature T_w
w = runback water
∞ = freestream

Introduction

ICE accretion on aircraft components in adverse weather conditions can jeopardize flight safety and affect aircraft performance. Because of its importance, various methods of ice protection have been developed. These can be classified in two broad categories: de-icing methods and anti-icing methods. *De-icing methods* deal with the intermittent removal, either by mechanical or thermal means, of any ice buildup by destroying the bond between the ice and the adjacent surface. *Anti-icing methods* are concerned with the prevention, or minimization, of ice buildup on particular surfaces. This is accomplished either by evaporating, or partially evaporating, supercooled water droplets that impinge on the surface. In the partial evaporation case, a portion of the impinging liquid water is allowed to run back aft of the thermally protected area and form an ice layer of thickness less than some prescribed, tolerable, amount. This so-called "runback" problem has also been observed on external aircraft surfaces in de-icing applications, but has not yet been analyzed.

Anti-icing methods generally involve chemical or thermal principles. Most of the current aircraft use thermal energy in the form of hot air or electrical energy in ice-protection sys-

Presented as Paper 89-0759 at the AIAA 27th Aerospace Sciences Meeting, Reno, NV, Jan. 9–12, 1989; received Jan. 14, 1989; revision received June 29, 1989.

*Graduate Student, Mechanical Engineering Department. Student Member AIAA.
†Professor, Mechanical Engineering Department. Associate Fellow AIAA.
‡Professor, Chemical Engineering Department.
§Senior Research Scientist. Member AIAA.
¶Manager. Member AIAA.

tems because these have proven to be most reliable. Systems that are used to protect engine inlets of turbine-powered aircraft are representative of the thermal type. In these applications, compressor bleed air is used to provide the required heating to a portion of the inlet surface.

The history of research in the anti-icing area is rather narrow. During the past several years, analytical studies have been confined to totally evaporative anti-icing systems, in which runback effects were ignored.[1,2] Research in partially evaporative anti-icing systems is quite basic and runback is treated in a primitive manner.

In the current study, a hot-air anti-icing system for a gas turbine engine inlet is analyzed. The engine nacelle is modeled as a number of flat panels through which the normal velocity is known or calculated to model the boundary-layer displacement (Fig. 1). The flowfield calculations, on and about the inlet surface, were performed using a three-dimensional potential flow code, VSAERO,[3] which accounts for compressibility effects. The results are alternately used in the calculations for the boundary-layer displacement thickness until convergence is met. Because each water droplet is subject to drag, buoyancy, and gravity forces, depending on its size, the droplet trajectory intersects the potential flow streamlines as the droplet approaches the inlet surface. Integration of the droplet trajectories is performed using a "local Stokes linearization" technique that proved to give stable and accurate results. The trajectory code also calculated local water collection efficiencies. The final step is the heat-transfer modeling of the engine cowl and the flowing water. The latter results in temperature distributions for particular conditions. In the following sections, each step of the process will be discussed in detail. Also, the results of a variety of test cases will be presented.

Particle Trajectory Analysis

Water impingement on two-dimensional and axisymmetric bodies has been studied for several years. However, droplet trajectory-code development for three-dimensional bodies has received only limited attention. Water-impingement studies on arbitrary inlet geometries have been presented by Norment,[4] Stock,[5] and Kim.[6] Basic features of a trajectory code generally consist of surface geometry definition, a potential flow solver, a velocity calculation, a trajectory integration technique, and collection-efficiency calculation.

Norment[4] used the panel code developed by Hess and Smith to calculate the potential flowfield. He modified the code to handle inlet flows although he also mentioned that the code was not organized to handle internal flows. Stock[5] used the finite-volume form of Eulers equations, and Kim[6] used Reyhner's full potential methods to define the potential flow. Panel methods are usually the least-expensive flow solvers because they require only a surface solution instead of a three-dimensional grid as required with finite-difference methods.

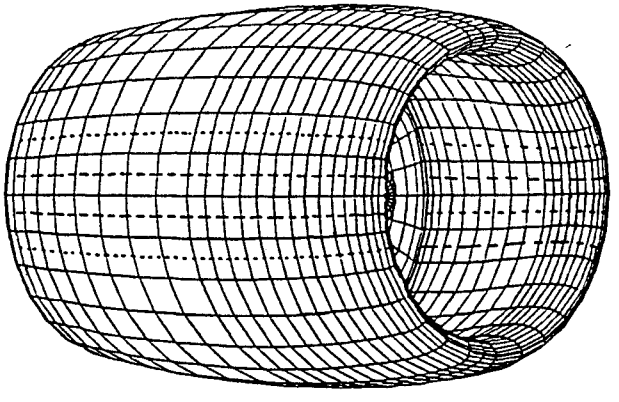

Fig. 1 Panel modeling of the nacelle surface geometry.

The velocity calculation for flow solvers that employ a three-dimensional grid[5,6] consists of interpolating the velocity at surrounding grid points for the velocity at the trajectory. Alternately, for panel methods, one can calculate the velocity directly by summing the contributions of all of the singularities representing the flow, as in Norment,[4] or one can calculate the velocities at all points on a regular three-dimensional grid from which the velocity may be interpolated. The latter, indirect method, is chosen for the present calculation because a large number of streamline trajectories were needed in the calculations, and because this approach separates the trajectory calculations from the panel method developed. Moreover, this leaves open the possibility of using other programs to generate the flowfield.

In this study, the surface geometry of the inlet is defined by means of flat panels. Kim[6] used curved panels, and, therefore, required a complex droplet/surface intersection procedure. Because the current flowfield code is a low-order one, many panels are typically used to represent the surface. Hence, the error due to the flat-panel approximation should not be significant.

To model the motion of each droplet, two assumptions were made:

1) Because of the small concentration of water droplets in the air, the flowfield is assumed to be undisturbed by the droplets.

2) The shape of each water particle is spherical.

The equation of motion of a single particle is obtained by applying Newton's second law:

$$m_d \frac{\mathrm{d}V_d}{\mathrm{d}t} = F_{\text{aero}} + F_{\text{buoy}} + F_{\text{grav}} \tag{1}$$

where

$$F_{\text{buoy}} = -\rho_{\text{air}}\, g(\pi/6)D_d^3 \tag{2}$$

$$F_{\text{grav}} = \rho_d\, g(\pi/6)D_d^3 \tag{3}$$

$$F_{\text{aero}} = -\tfrac{1}{2}\rho_{\text{air}}\, S\,|V_{\text{rel}}|\,V_{\text{rel}}\, C_D \tag{4}$$

In the latter expression,

S = the projected area, $\pi D_d^2/4$, of the droplet
V_{rel} = the relative velocity between the air and the droplet
C_D = the drag coefficient, which is a function of V_{rel} and the droplet size

In the present method, values of C_D are taken from White.[7] It should be mentioned that the form of Eq. (4) is only a definition of C_D, which is preferred because, at high Reynolds numbers, C_D is nearly constant for small changes in velocity. For small Reynolds numbers, Stokes[8] showed that the drag coefficient is

$$C_D = \text{const}/|V_{\text{rel}}| \tag{5}$$

The latter equation can be extended to very high Re if the calculated drag is recognized to be accurate for a small range of relative velocities, i.e., if

$$C_{Do} = [|V_{\text{rel}}|C_D]_{V_{\text{rel}}(t_o)} \tag{6}$$

one can write (local Stokes linearization)

$$F_{\text{acro}}(t) = -\tfrac{1}{2}\,\rho_{\text{air}}\, SV_{\text{rel}}C_{Do} \qquad t_o < t < t_o + \Delta t \tag{7}$$

where Δt is a small time step. Hence, only a small error in the drag will be introduced. In practice, Re (and therefore V_{rel}) is high and rapidly changing only very close to the body where small time steps are also required to ensure an accurate trajectory. Using the definition for the relative velocity,

$$V_{\text{rel}} = V_d - V_{\text{air}} \tag{8}$$

and substituting Eqs. (2), (3), and (7) into Eq. (1) yields the equation of motion of a single particle:

$$\frac{dV_{rel}}{dt} = -\frac{1}{m_d}\rho_{air}\frac{\pi}{8}D_d^2 C_{Do} V_{rel} + \frac{1}{m_d}\frac{\pi D_d^3}{6} g(\rho_d - \rho_{air}) - \frac{dV_{air}}{dt} \tag{9}$$

where dV_{air}/dt is the apparent change in the air velocity as seen by the droplet. Assuming that the following quantities are constant within a time step, but change from one time step to the next,

$$E = \frac{1}{m_d}\frac{\pi D_d^3}{6} g(\rho_d - \rho_{air}) - \frac{dV_{air}}{dt} \tag{10}$$

$$B = \frac{1}{m_d}\rho_{air}\frac{\pi}{8}D_d^2 C_{Do} \tag{11}$$

Equation (9) can then be written as

$$\frac{dV_{rel}}{dt} + BV_{rel} = E$$

The solution to this is

$$V_{rel}(t) = C^* e^{-Bt} + (E/B) \tag{12}$$

where the constant C^* is chosen to satisfy the condition that the relative velocity at the beginning of any step size equals the relative velocity at the end of the previous time step. Once the relative velocity is known, the position of the droplet can be found relative to a streamline passing through the same initial point. The particle trajectory solution is performed after generating air velocity data from the panel and boundary-layer solutions. The validity of the code will be shown in the Results and Discussion section.

The Federal Aviation Administration (FAA) regulations[9] define the continuous and intermittent icing conditions that an aircraft must be able to operate safely within if it is to be certified for flight into forecast icing conditions. These conditions are the ambient air temperature, the cloud liquid water content, and the droplet mean effective diameter. The liquid water content LWC is the mass of water contained in a unit volume of air. The random size water droplets in a cloud are described statistically by their mean effective diameter (MED), typically measured in microns. Droplet mean diameters from 10 to 50 μm are common in icing conditions.

When an airplane flies through a cloud, airborne water droplets impinge on the leading edges of wings, nacelle, etc. Ahead of the airplane, the freestream flux of water is

$$W_\infty = \mathrm{LWC}V_\infty \tag{13}$$

The collection efficiency β at a point on the aircraft surface is defined as the local water-impingement rate divided by the freestream flux,

$$\beta = W_{local}/W_\infty \tag{14}$$

It is standard practice to assume that droplets do not interact with each other so that a collection-efficiency calculation is valid for all values of the liquid water content. In the present method, the collection efficiency of a panel representing the surface is determined by finding the droplet trajectories which impact at the four corner points of the panel, as illustrated in Fig. 2. Consequently, the definition of the collection efficiency is altered to read

$$\beta = A_\infty/A_p \tag{15}$$

Another advantage of this approach is that it can be shown that the sum of the collection rates of the surface panels is equal to the total water flux removed from the freestream.

Heat Transfer Analysis

An accurate model that represents the various modes of heat transfer occurring in an anti-icing system will now be developed. The model can be used for performance predictions and/or in parametric studies where the problem variables are difficult to control, e.g., in flight or in tunnel experiments. The latter can be very expensive if an extensive test agenda is required. Use of analytical techniques implies that experimental studies for only a few general cases need be conducted in order to determine the validity of the theoretical model.

Formulation of a method for calculating runback water and the surface temperature distribution is based on the following arguments and assumptions:

1) Since the runback water-film thickness and the thickness of the metal skin are both very small compared with the length in the direction of flow, variation of temperature in the transverse direction, i.e., normal to the cowl surface, will be neglected.

2) The magnitude of heat transfer in the circumferential direction is much smaller than that in the flow direction. This allows one to consider a one-dimensional problem at several angular locations along individual streamlines.

3) Because the Péclet number ($Re\ Pr$) in the water layer is large, the axial conduction heat transfer component within the energy equation for the water is negligible compared to the other equation components.

4) All of the physical properties in the energy-balance equations are constant.

5) The anti-icing system has been operating long enough so that all transients have vanished and the system is in steady state.

Energy Balance on the Metal Skin

Consider the control volume shown in Fig. 3. An energy balance produces

$$h_i(T_a - T_{sk}) - h_\infty(1-F)\left[T_{sk} - \left(T_e + \frac{\eta_r V_e^2}{2g_c J C_{p_{air}}}\right)\right] - h_w F(T_{sk} - T_w) + \frac{K_{sk}}{Y_i}\frac{d}{dx}\left[A_{sk}\frac{dT_{sk}}{dx}\right] = 0 \tag{16}$$

where the first term represents the convective heat transfer from the hot bleed air to the skin; the second and third terms, the convective heat loss from the metal skin to the external airstream in the dry region (surface not wetted by runback water) and to the runback water in the wet region (surface wetted by runback water), respectively; and, the fourth term, the heat conduction in the metal skin in the flow direction.

In Eq. (16), F is the wetness factor, which is defined as the fraction of the skin perimeter, at a given location, that is

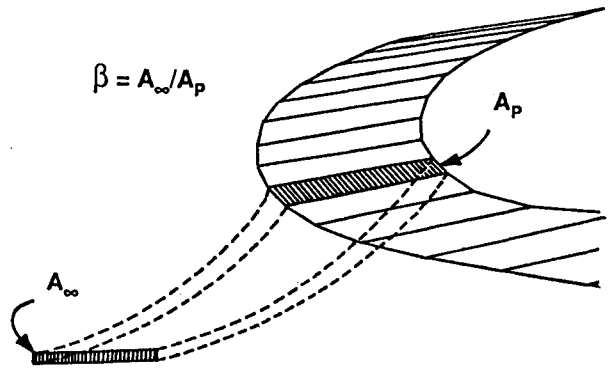

Fig. 2 Panel-by-panel collection-efficiency calculation.

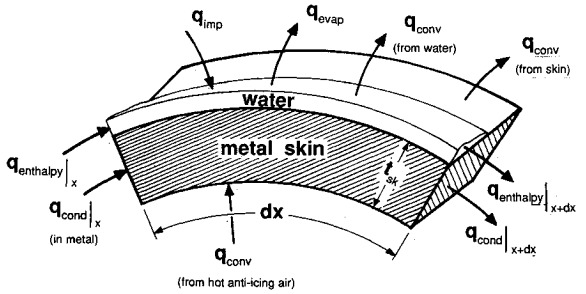

Fig. 3 Energy balance on the metal skin and the runback water.

wetted by the runback water. In regions of direct water impingement, the surfaces are fully wetted and F takes a value of unity. In general, this occurs at the leading edges of wings, airfoils, the lip of an engine cowl, etc. Downstream of these regions, the water breaks up into individual rivulets that tend to decrease in width. In this case, the factor F can reach a value[2] of approximately 0.2.

The term η_r in Eq. (16) denotes a temperature recovery factor for the air outside the wall boundary layer. This factor can be approximated by[10]

$$\eta_r = 1 - \frac{V_e^2}{V_\infty^2}(1 - Pr_{\text{air}}^n), \quad n = \begin{cases} \frac{1}{2} & \text{for laminar flow} \\ \frac{1}{3} & \text{for turbulent flow} \end{cases} \tag{17}$$

In general, the effect of the heat conduction within the skin in the flow direction is negligible in comparison with the heat flow in the transverse direction. This allows one to rewrite Eq. (16) as follows:

$$T_{sk} = \frac{h_i T_a + h_w F T_w + h_\infty (1-F)\left[T_e + \dfrac{\eta_r V_e^2}{2g_c J C_{p\,\text{air}}}\right]}{h_i + h_w F + h_\infty (1-F)} \tag{18}$$

If the conduction term in Eq. (16) is retained, the skin temperature cannot be explicitly determined. Instead, a second-order ordinary differential equation is produced.

Mass and Energy Balance on the Runback Water

A mass balance on the runback water yields

$$\frac{dm^o}{dx} = Y_o(W_{\text{imp}} - W_{\text{evap}}) \tag{19}$$

where the rate of impingement per unit area W_{imp} is computed using the local value of the collection efficiency as follows:

$$W_{\text{imp}} = \beta \text{LWC} V_\infty \tag{20}$$

The evaporation rate per unit area can be shown to be

$$W_{\text{evap}} = \frac{h_\infty}{C_{p\,\text{air}}}\left(\frac{Pr}{Sc}\right)_{\text{air}}^{2/3} \frac{M_{H_2O}}{M_{\text{air}}}\left[\frac{P_{v,w} - P_{\text{vap}}}{P_e - P_{v,w}}\right] \tag{21}$$

where P_{vap} is the local vapor pressure at the edge of the boundary layer at the local relative humidity.

Application of Dalton's Law of partial pressures and knowledge of ambient conditions yields

$$P_{\text{vap}} = P_e \frac{P_{v,\infty}}{P_\infty} \phi_\infty \tag{22}$$

Generally, the relative humidity ϕ_∞ in a cloud is taken to be 100%. The saturation vapor pressure of pure liquid water has been expressed as a function of water temperature T_w in the range of interest as

$$P_v(T) = 2337 \exp\left\{6789\left[\frac{1}{293.15} - \frac{1}{T}\right] - 5.031 \ln\left[\frac{T}{293.15}\right]\right\} \tag{23}$$

where the units of P_v and T are pressure (Pa) and degrees Kelvin (K), respectively.

Now, performing a heat balance on the water control volume shown in Fig. 3 gives

$$h_w(T_{sk} - T_w) - h_\infty\left[T_w - \left(T_e + \frac{\eta_r V_e^2}{2g_c J C_{p\,\text{air}}}\right)\right] + W_{\text{imp}} C_{p_w}(T_\infty - T_w) + \frac{W_{\text{imp}} V_o^2}{2g_c J} W_{\text{evap}} L_v - \frac{C_{p_w}}{Y_o F}\frac{d}{dx}[m^o(T_w - T^*)] = 0 \tag{24}$$

It was assumed that the droplet temperature remains at its ambient atmospheric cloud value before striking the cowl surface. Using Eq. (19) in (24) and rearranging terms yields

$$\frac{dT_w}{dx} = \frac{Y_o F}{m^o C_{p_w}}\left\{-[h_w + h_\infty + C_{p_w}(2W_{\text{imp}} - W_{\text{evap}})]T_w + h_w T_{sk} + h_\infty\left[T_e + \frac{\eta_r V_e^2}{2g_c J C_{p\,\text{air}}}\right] + W_{\text{imp}} C_{p_w} T_\infty + \frac{W_{\text{imp}} V_o^2}{2g_c J} - W_{\text{evap}} L_v + \frac{C_{p_w}}{F}(W_{\text{imp}} - W_{\text{evap}})T^*\right\} \tag{25}$$

Thus far, no mention has been made regarding the runback film thickness or its flow velocity. In order to evaluate the local heat transfer coefficient between the metal skin and the runback water, a velocity distribution of the water film is required. It is expected that this velocity is a function of position along the surface because at the stagnation point on the cowl surface its value is zero. From this point onwards, the water is accelerated due to aerodynamic forces. From a boundary-layer analysis, the local friction coefficient f at the surface of the cowl was obtained. By definition, the corresponding local wall shear stress τ_w is then computed from

$$\tau_w = f(\gamma P M^2/2) \tag{26}$$

Because the film thickness is very small, the water velocity v_w is assumed to vary linearly with y at a given location along the surface, such as would be found in a pure shear flow. Also, it is assumed that the flow is caused due to the shearing force τ_w, which is imposed on the upper boundary of the film. Using the conventional no-slip condition at the lower boundary, the water velocity may be expressed as

$$v_w(x,y) = [\tau_w(x) y/\mu_w]$$

The above equation can be integrated over the film thickness to give a mean velocity

$$V_w(x) = [\tau_w(x) t_w/2\mu_w] \tag{27}$$

The film thickness t_w can be written as

$$t_w = m^o/\rho_w Y_o V_w F \tag{28}$$

Combining Eqs. (27) and (28) yields

$$V_w = \left[\frac{\tau_w m^o}{2\mu_w \rho_w Y_o F}\right]^{1/2} \tag{29}$$

The water velocity may now be used to compute a local Reynolds number. In turn, this value may be used in relations for the heat transfer coefficient. To accomplish this, it was assumed that the actual flow was the same as that for a flat plate.

Another important use of V_w is in locating the point where the runback water begins to freeze. When a particle of liquid

water flowing over the unprotected region reaches a temperature of 0°C, it will remain at 0°C until it gives up all its latent heat L_f at some location x^* where it turns into an ice particle. Clearly, the value of x^* depends on the speed of that particle. A slight variation in Eq. (25) will give the amount of energy lost per unit time. This, along with the velocity V_w, can be used to compute the net loss of energy between the 0°C liquid point and another point downstream. Then, a comparison with L_f is made. This concept and numerical integration are used to predict the location x^*.

Numerical Methods of Solution

The governing equations to the heat-transfer problem are Eqs. (19) and (25) for the case where axial conduction within the metal skin is neglected. For the case where the conduction term is retained, Eq. (16) as well as Eqs. (19) and (25) are the governing equations. All of these equations are first-order and second-order ordinary differential equations (ODE) and have to be solved simultaneously. Because of the arbitrary distribution of many terms in the above equations, an analytical form of solution was impossible. The fourth-order Runge-Kutta numerical technique[11] was used. This method requires the specification of an initial value for the parameter to be solved for. Appropriate values for T_w, T_{sk}, and m^o were chosen at the stagnation point. However, in the case where the skin axial conduction was retained, a second-order ODE was obtained, i.e., Eq. (16). Following the usual procedure, this equation was written as two first-order ODEs. The two initial values used in the solution were a prescribed temperature and an assumed value of temperature gradient that would lead to a prescribed temperature at a specified location downstream. In this case, the shooting method (trial and error) version of the Runge-Kutta method was used.

Results and Discussion

Verification of the trajectory code was accomplished by considering three test cases. Test runs were made to determine the trajectories of both very small and very large droplets. The smallest droplets (MED = 1 μm) had the same trajectories as the flow streamlines, while the largest droplets (MED = 1000 μm) had trajectories which followed straight paths in the absence of gravity. These results were expected. In a second test case, Kim's calculations[6] for the paths of 0.1- and 14.7-μm droplets near a sphere were found to be indistinguishable from those computed via the present method; see Fig. 4.

A third set of test cases were used to verify the trajectory calculations for a NACA 0012 airfoil with a chord length of 13 in. at 0-deg angle of attack. These test cases were run by several of the participants at the Droplet Trajectory Workshop recently held at the NASA Lewis Research Center. Results were compared to test data obtained in the NASA Lewis Icing Research Tunnel. The results of the current study are contrasted to this data in Fig. 5. The numerical predictions and the experimental results are seen to be in quite good agreement.

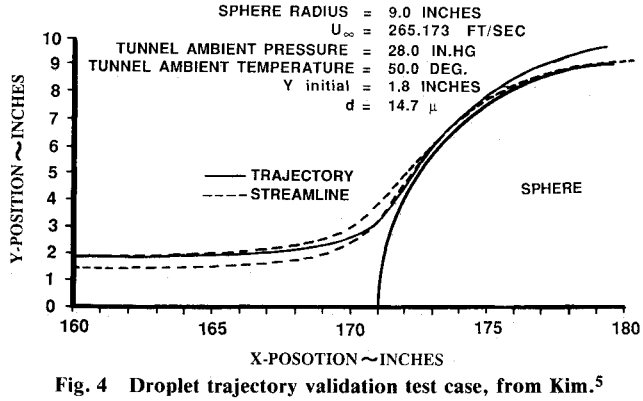

Fig. 4 Droplet trajectory validation test case, from Kim.[5]

An axisymmetric nacelle geometry was considered for the purpose of illustrating a few sample icing calculations. The cross section of the nacelle, passing through the centerline axis, is shown in Fig. 6. Four natural icing cases were considered (Table 1), but only the results of cases 1 and 4 are illustrated. Results of cases 2 and 3 are shown in Ref. 12. These cases were chosen because they represent the worst conditions for each of the flight conditions: hold, climb, cruise, and descent.

The mean effective diameter (MED) of water droplets in a cloud may be chosen from within ranges established in the Federal Aviation Regulations[9] (FAR). The MED ranges are 15–40 μm for continuous maximum (stratiform clouds) atmospheric icing conditions, and 15–50 μm for intermittent maximum (cumuliform clouds) atmospheric icing conditions. Past studies and experience have shown that, for a given set of aircraft flight conditions and atmospheric conditions, the overall collection efficiency is maximum when using the Langmuir "D" distribution of water droplets with a MED of 20 microns. This value of MED was used to yield more conservative results.

In each of the four cases, the data given in Table 1 along with the nacelle geometry and the engine inlet airflow rate were used in the potential flowfield and boundary-layer calculations. The latter result in distributions on a well-defined grid of the local velocities, the local pressure coefficient, and the friction coefficient at the cowl surface.

The flowfield data and atmospheric icing conditions were next used to calculate trajectories of individual droplets. Collection efficiencies and corresponding impingement rates for each panel were then calculated using methods previously discussed. Consequently, water-impingement flux distributions were obtained. Figure 7 is a plot of this distribution for case 1 conditions. In this figure, the *wrap distance* is measured from the nose lip highlight of the cowl along the surface following a streamline, and is positive in the inboard flow direction.

The external heat transfer coefficient distribution, between the ambient air and the outer surface of the cowl, and the internal heat transfer coefficient distribution, between the hot anti-icing air (compressor bleed air) and the inner surface of the cowl, directly affect the magnitude of the runback water temperature. Therefore, these two parameters must be determined as accurately as possible. Because of the complexity of the flow of the anti-icing air inside the irregular cowl duct shapes, the internal heat transfer coefficients were calculated based on experimental testing. However, the external heat-transfer coefficients were calculated by assuming that the cowl consists of a cylinder at the leading edge followed by a flat plate. Semiempirical relations were then used in the calculations assuming that the flow is turbulent in the flat plate region. This was done in order to be more conservative in the performance analysis.

During the numerical investigation, it was found that the rate of evaporation from the runback water significantly affected the runback water temperature. Evaporative cooling in this type of problem is very important for two reasons. First,

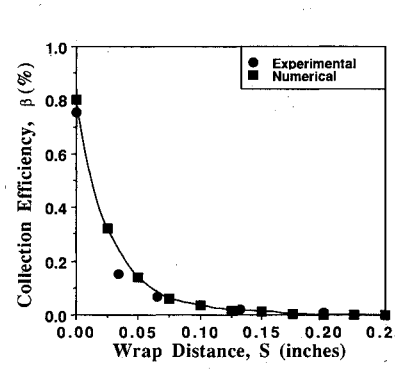

Fig. 5 Collection efficiency of a NACA 0012 airfoil.

Table 1 Flow conditions for sample cases

	Case 1	Case 2	Case 3	Case 4
Condition	Hold[a]	Climb[b]	Cruise[b]	Descent[a]
Altitude, ft	15,000	5000	22,000	1500
M_∞	0.48	0.41	0.6	0.38
T_∞, °C	− 12.22	− 12.22	− 30.00	− 10.00
P_∞, KPa	58.1	86.9	44.7	97.0
T_{air}, °C	276	384	298	177
MED, μm	20	20	20	20
LWC, g/m^3	0.38	0.38	0.14	0.42

[a]Continuous maximum icing conditions. [b]Intermittent maximum icing conditions.

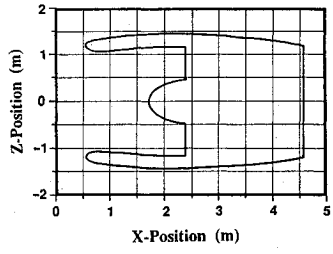

Fig. 6 Cross section of an axisymmetric nacelle model.

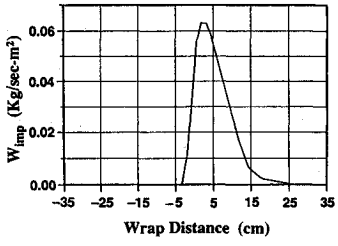

Fig. 7 Rate of water-impingement flux distribution (case 1).

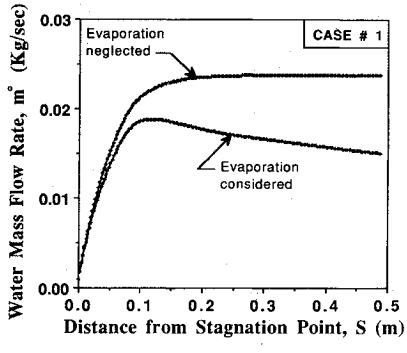

Fig. 8 Runback water mass flow rate distributions (case 1).

the rate of mass evaporated is the same order of magnitude as the total mass flow rate downstream of the impingement region. This is due to the large surface area of the runback water that is exposed to the ambient air, and because of the very small thickness of the water layer. Second, evaporative cooling is important because of the relatively large value of the water latent heat of vaporization. Figure 8 shows the effect of evaporation on the water mass flow rate along the cowl surface for case 1. Correspondingly, Figs. 9 and 10, respectively, show the metal skin and water temperatures when evaporation is neglected and when evaporation is taken into account. As may be seen, evaporative cooling of the runback water has a great tendency to decrease the runback water temperature. The mass flow rate, the metal skin temperature, and the runback water temperature distributions for case 4 are illustrated in Figs. 11 and 12.

In general, it is desirable to evaporate as much of the impinging water as possible to keep the amount of water

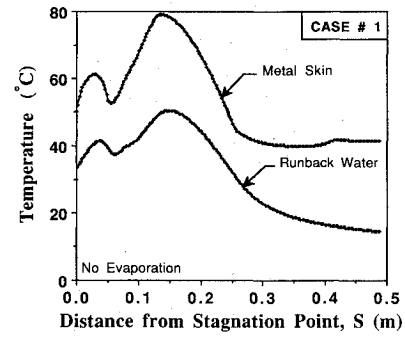

Fig. 9 Temperature distributions neglecting evaporation (case 1).

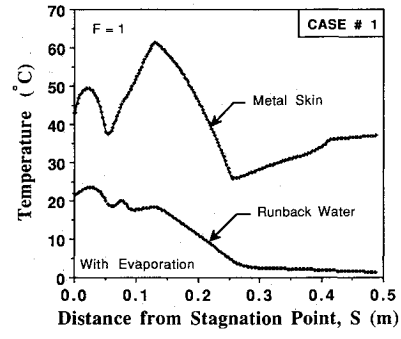

Fig. 10 Temperature distributions accounting for evaporation (case 1).

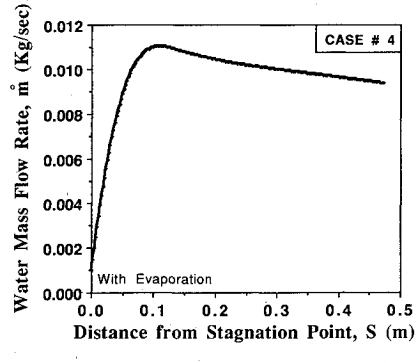

Fig. 11 Runback water mass flow rate distribution (case 4).

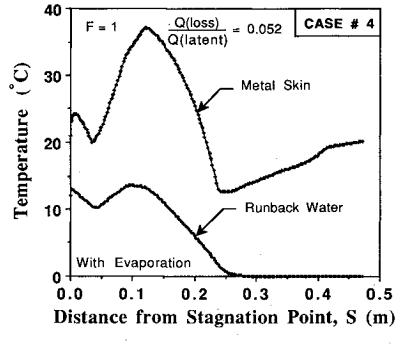

Fig. 12 Temperature distributions (case 4).

flowing towards the fan face as small as possible, especially if these downstream regions are thermally unprotected. The tradeoff here is that any increase in anti-icing power supplied leads to a slight decrease in engine power. Consequently, the design of an anti-icing system should be based on performance and economic considerations of both the anti-icing system and the aircraft engine.

In case 4, the water reached a temperature of 0°C but did not become a solid. The ratio of heat loss to the latent heat is shown in Fig. 12 at a distance of $S = 0.472$ m.

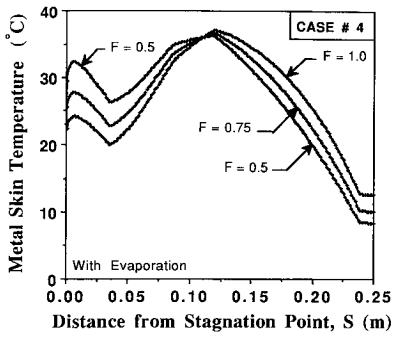

Fig. 13 Effect of wetness factor on the metal skin temperature distribution.

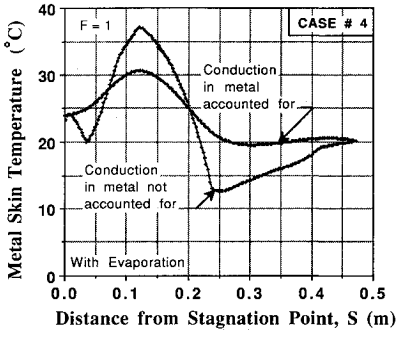

Fig. 14 Effect of axial conduction in the wall on the metal skin temperature.

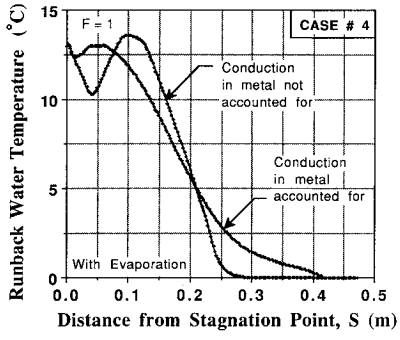

Fig. 15 Effect of axial conduction in the wall on the runback water temperature.

The effect of wetness factor F was also investigated. Figure 13 shows sample calculations using the conditions described for case 4. It is seen that a decrease in the wetness factor tends to slightly decrease the metal skin temperature because it becomes directly exposed to the cold ambient air. This also affects the runback water temperature in a similar fashion.

The conduction of heat within the metal skin in the flow direction was neglected in all of the previous calculations. It has been general design practice to neglect this term. However, if the conduction term is retained, Eq. (16) must be solved simultaneously with Eqs. (19) and (26) instead of explicitly using Eq. (18). Because Eq. (16) is a second-order ordinary differential equation, two boundary conditions are required. Since no previous knowledge of the downstream skin temperature at a specified location is available, the boundary conditions used are those given at $S = 0$ and $S = 0.472$ m from the solution, which does not account for the conduction term. Figures 14 and 15 reveal that conduction may be neglected and its major effect is in damping the oscillations in the results due to the oscillations in the internal heat transfer coefficients.

Conclusions

In this paper, a computational method was developed to analyze the anti-icing system used to protect a jet engine inlet. The method incorporates a potential flow panel code for flowfield computation, a water droplet trajectory code for impingement-rate estimation, and energy balances on the runback water and the metal skin of the nacelle for prediction of the corresponding temperature distributions. It was found that accurate prediction of water-impingement rates and the heat transfer coefficients is essential to the evaluation of the anti-icing system.

It was shown that a fairly large amount of heat from the anti-ice air should be concentrated in the stagnation-point region where direct impingement occurs. This assures that the water droplets remain in a liquid state and also causes some of the water to evaporate. It is recommended that the region aft of the heated area should also be moderately protected. The water could reach the freezing temperature in this zone even though the metal skin may exist at a relatively higher temperature. Previous investigations have only considered the energy balance of a wetted metal skin without separately considering the energy balance of the runback water.

It was found that the decrease in wetness factor tends to slightly decrease the wall, as well as the runback water, temperature, depending on the meteorological and flight conditions. This was observed only in regions where the net rate of heat loss was larger than the net rate of heat gain, in absolute values. Individual streams or rivulets have been observed in actual flights and in tunnel tests. Wetness factor distributions may be obtained from the latter and included in the system performance computations.

Acknowledgment

The present investigation was sponsored in part by the General Electric Company and the NASA Lewis Research Center.

References

[1]Pfeifer, G. D., "Aircraft Engine Icing Technical Summary," *Ice Test for Aircraft Engines,* AGARD CP 236, 1978.

[2]*SAE Aerospace Applied Thermodynamics Manual,* Pt. 3F, Society of Engineers, Warrendale, PA, 1969, pp. 358–387.

[3]Maskew, B., "Prediction of Subsonic Aerodynamic Characteristics: A Case for Low-Order Panel Methods," *Journal of Aircraft,* Vol. 19, No. 2, 1982, pp. 157–163.

[4]Norment, H. G., "Calculations of Water Drop Trajectories to and about Arbitrary Three-Dimensional Lifting and Nonlifting Bodies in Potential Airflow," NASA CR-3935, Oct. 1985.

[5]Stock, H. W., "Water Droplet Trajectory Computation around an Air Intake," *Zeitschrist fur Flugwissenschaften und Weltraumforschung,* Vol. 8, No. 3, 1984, pp. 200–208.

[6]Kim, J. J., "Particle Trajectory Computation on a Three-Dimensional Engine Inlet," NASA CR-175023, Jan. 1986.

[7]White, E. B., *Viscous Fluid Flow,* McGraw-Hill, New York, 1974, pp. 204–210.

[8]Stokes, G. G., "On the Effect of the Internal Friction of Fluids on the Motion of Pendulums," *Transactions of the Cambridge Philosophical Society,* Vol. 9, Pt. II, 1851, pp. 8–106.

[9]"Transport Category Airplanes," Federal Aviation Regulations, Airworthiness Standards, Pt. 25, Appendix C, Federal Aviation Administration, Washington, DC, 1982.

[10]Gelder, T. F., and Lewis, J. P., "Comparison of Heat Transfer from Airfoil in Natural and Simulated Icing Condition," NACA TN-2480, Sept. 1951.

[11]Carnahan, B., Luther, H. A., and Wilkes, J. O., *Applied Numerical Methods,* Wiley, New York, 1969, pp. 363–366.

[12]Al-Khalil, K. M., Keith, T. G., De Witt, K. J., Nathman, J. K., and Dietrich, D. A., "Thermal Analysis of Engine Inlet Anti-Icing Systems," AIAA Paper 89-0759, Jan. 1989.